Aalto University

Kerminen, Juho; Xie, Boxuan; Mela, Lauri; Karakoç, Alp; Ruttik, Kalle; Jäntti, Riku

Low-cost thin film patch antennas and antenna arrays with various background wall materials for indoor wireless communications

Low-cost thin film patch antennas and antenna arrays with various background wall materials for indoor wireless communications

View the article online for updates and enhancements.

Flexible and Printed Electronics

PAPER

Low-cost thin film patch antennas and antenna arrays with various background wall materials for indoor wireless communications

Juho Kerminen[1] , Boxuan Xie[1,*] , Lauri Mela , Alp Karakoç , Kalle Ruttik and Riku Jäntti

Department of Information and Communications Engineering, Aalto University, 02150 Espoo, Finland
[1] Equally contributed.
[*] Author to whom any correspondence should be addressed.

E-mail: boxuan.xie@aalto.fi

Keywords: flexible antenna, antenna array, inkjet printing, solderless, wireless communication, IoT, MIMO

Abstract

The present study introduces an inkjet-printed flexible coplanar waveguide patch antenna array concept. Single antenna and four-element antenna arrays were characterized, which were attached to a subminiature version A connector via an innovative solderless, 3D-printed 'plug-and-play-type' tightener. Furthermore, indoor wireless communication and Internet of Things scenarios with commonly used wall materials including gypsum and plywood boards, on which patch antennas and antenna arrays can be attached, were also presented. In order to validate the concept, design and fabrication iterations in parallel with numerical and experimental investigations were executed. To elaborate, single antenna and antenna array configurations without and with wall materials were characterized to see their functionality at 2.4 GHz resonance frequency and beyond 300 MHz bandwidth, respectively. The results demonstrate that the investigated configurations fulfill short-range radio transmission and can be utilized, e.g., for indoor backscattering-type communications and wireless sensing applications, as an affordable and versatile alternative to their conventional counterparts. Being attached to their corresponding background materials, single-antenna specimens were measured to have return losses beyond 18 dB and peak gains around 1 dBi, while higher peak gains above 6 dBi were detected for antenna arrays. Moreover, the antenna arrays can enable multiple-input and multiple-output communication. The proposed arrays had diversity performance in terms of return losses higher than 15 dB, isolation of more than 20 dB, envelope correlation coefficient < 0.001, diversity gain > 9.95 dB, mean effective gain < -3 dB, power ratio factor < 0.5 dB, and channel capacity loss < 0.4 bits/s/Hz.

1. Introduction

The recent rapid growth of the 5G and Internet-of-Things (IoT) infrastructure is contributing to the massive interconnection of the digital and physical worlds. Meanwhile, the flexible radio frequency (RF) components with low-complexity and low-cost features are becoming increasingly popular [1–3]. As a significant part of such RF devices, antennas printed on ultra-thin flexible substrates take advantage of lightweightness, bendability, and compatibility with various digital device technologies. Conventional patch antennas fabricated using micro-electronics have been widely used for IoT devices [4, 5] while the direct writing and additive manufacturing methods have been also gaining ground with their increasing yield and repeatability [6, 7]. Especially, in recent

years, inkjet printing technology, which has low-cost yet high resolution, has become a popular thin film electronics fabrication method [8]. This allows rapid and drop-on-demand manufacturing of conductive and radiating elements such as antennas on compliant substrates.

For instance, Khaleel *et al* proposed a compact inkjet-printed coplanar waveguide (CPW) antenna, which was printed on polyimide substrate with silver nanoparticle ink, for ultra-wideband (UWB) wireless applications [9]. Similarly, Casula *et al* developed an inkjet-printed antenna with a custom topology for passive radio frequency identification (RFID) communication [10]. In their study, the antenna was fabricated with silver nanoparticle ink and a polyethylene terephthalate (PET) substrate. Shastri *et al* implemented a similar ink–substrate combination to

investigate the frequency-reconfigurable patch antennas, for which capacitors and diodes were affixed onto the printed aperture using conductive adhesives [18]. Thus, they were able to switch and tune the antenna operating frequency.

Furthermore, an inkjet-printed RFID tag antenna for sensor applications was also demonstrated by Islam *et al* [13]. Their configuration consisted of a modified meander line radiator with a semi-circular-shaped feed network, the antenna of which was printed on a photo paper with silver nanoparticle ink. Saha *et al* also used photo paper as a substrate in their investigations, through which an inkjet-printed UWB antenna was presented [21]. The antenna pattern comprises a circular patch with a double-stepped symmetric ground plane and was fed by a CPW technique on one-sided photo paper. Recently, Abutarboush demonstrated the capabilities of the inkjet-printing method, where custom-shaped antennas were printed on synthetic paper with silver nanoparticle ink [20]. The antenna bending tests were carried out to validate the mechanical durability and to measure the peak gains and efficiencies that were deduced to be in the ranges from −3 to 2 dBi and 40%–60%.

Apart from metallic conductive inks, graphene inks have also been investigated for printing purposes in the literature. For instance, Labiano *et al* proposed an inkjet-printed graphene-based flexible CPW antenna working in the frequency range of 5–6 GHz [17]. In addition to the single antenna studies, researchers further investigated inkjet-printed graphene-based antenna arrays. For instance, 1×2 phased array antenna by Monne *et al* was demonstrated for the radio beam steering applications [23]. Graphene-based field-effect transistors were used as switches in the delay line of the antenna. Khinda *et al* proposed an inkjet-printed two-element patch antenna array [24]. The stability of its RF performance was evaluated after several mechanical stress cycles.

In addition to inkjet printing, there have also been other printing techniques for flexible antenna fabrication, such as screen printing, 3D printing, etc. For example, Kazani *et al* demonstrated screen-printed wearable patch antennas on several textile substrates using silver-based conductive inks [11]. They further covered the printed antennas with a protective thermoplastic polyurethane (TPU) layer to make the antenna washable and durable. In a similar fashion, screen printing was used by Adami *et al* to demonstrate a 2.45 GHz microstrip patch rectenna that was printed with silver ink on polyester/polycotton [12]. Furthermore, as listed and elaborated in table 1, there have been various innovative fabrication techniques for flexible antennas by Zhang *et al* [16], Sindhu *et al* [19], Li *et al* [14], Yin *et al* [15] to name a few.

Moreover, several investigations were also conducted on flexible antenna arrays that implemented different fabrication procedures than inkjet printing. In their studies, Biswas and Chakraborty [22] and Dey *et al* [27] fabricated two-element wearable multiple-input multiple-output (MIMO) antennas with copper conductive layers and jeans cloth substrates. In both designs, two stubs were mounted in the middle position located on the backside of the antenna and attached to the partially etched ground to enhance the characteristics of port isolation. A textile 2.4 GHz 2×2 rectenna array using a microstrip patch topology for RF energy harvesting was demonstrated by Lopez-Garde *et al* for which the conductive layer was glued on the felt substrate [25]. Another 1×4 patch antenna array based on a flexible mesh-style conductive fabric and E-glass fiber substrate was demonstrated by Elmobarak *et al* for wireless applications at the 5.8 GHz band [26]. Jayant *et al* also investigated four-port flexible UWB MIMO antennas for wearable IoT applications and reported their radiation performance when integrated into footwear [28]. The configuration, fabrication, and application details for the above-mentioned investigations and our proposed designs with their performance metrics are also provided in table 1 for single antennas, and in table 2 for antenna arrays.

It is worth noting that inks and substrates are of critical importance for inkjet-printed antennas. For several decades, researchers have been investigating a wide variety of inks based on e.g., silver, carbon, and copper, and their interactions with the substrates in consideration of their performance [29–31]. Nonetheless, there have been several investigations of the commonly used substrates such as paper, polyimide, PET, and TPU [29, 32, 33]. It has been demonstrated that the performance of the printed antennas is affected by multiple factors, such as surface roughness and dielectric characteristics of substrates, conductive characteristics of inks, as well as post-printing processes, such as thermal, photonic, and plasma sintering, etc, which ensures adhesion of the ink on the substrate [24].

However, to the authors' best knowledge, the effect of background wall materials, on which the thin film patch antennas are attached, the performance of inkjet-printed antennas have not been clearly identified in the literature. In order to investigate this metric, we introduced a solderless (plug and play type of fixture), thin-film printed patch antenna design operating at 2.4 GHz industrial, scientific and medical (ISM) frequency band, which is a good candidate for short-range radio transmission, especially in the case of indoor IoT and backscatter communications, as well as wireless sensing applications. The investigations with such solderless configuration not only facilitated repeatable experimental data for the performance metrics but also demonstrated modular and easy-to-use antenna setups.

Table 1. A comparison of the proposed antennas with other flexible antennas.

Reference	Freq. (GHz)	Material		Size (mm²)	Topology	Antenna			BW (MHz)	Application
		Conductive	Dielectric			Gain (dBi)	Efficiency (%)			
			Construction							
[9]	2.2–14.3	Silver nanoparticle	Kapton	Inkjet printing	33 × 47	CPW patch	1.7	N/A	Ultra-wide	IoT, UWB
[10]	0.86–0.96	Silver	PET	Inkjet printing	57.2 × 80.9	Custom	1.9 ± 0.15	N/A	300	RFID
[11]	2.45	Silver	Woven textile	Screen printing	42.5 × 48.5	Microstrip patch	N/A	N/A	N/A	IoT, WBAN
[12]	2.45	Silver	PES/cotton	Screen printing	42.1 × 33.1	Microstrip patch	N/A	N/A	N/A	IoT
[13]	0.86–0.96	Silver nanoparticle	Paper	Inkjet printing	44 × 59	Custom	2.12	N/A	300	RFID
[14]	2.45	Conductive fabric	NinjaFlex	3D printing	32.3 × 32.3	Microstrip patch	1.8	30.7	269.5	WBAN
[15]	2.45	Conductive textile	Rogers laminate	N/A	18 × 18	Custom	2.2	N/A	150	WBAN
[16]	4.8–5.9	Copper mesh	Air	N/A	36 × 28.7	Microstrip patch	7	N/A	900	WLAN
[17]	5–6	Graphene	Kapton	Inkjet printing	20 × 30	CPW patch	−0.95	42	3000	Wearable IoT
[18]	2.2/2.6	Silver nanoparticle	PET	Inkjet printing	61.9 × 44.7	Custom	3.9/4.7	N/A	374/624	WLAN, sensing
[19]	5.8	Mxene	Polyimide sheet	Laser cutting	17.23 × 13.3	Microstrip patch	−6.14	N/A	100	IoT
[20]	1–6	Silver nanoparticle	Synthetic paper	Inkjet printing	37.4 × 9.5	Custom	−3 to +2	40–60	N/A	IoT
[21]	3.2–30	Silver nanoparticle	Photo paper	Inkjet printing	33.1 × 32.7	CPW patch	4.87	86.61	Ultra-wide	IoT, UWB
Air-design	2.4	Silver nanoparticle	PET	Inkjet printing	34 × 42	CPW patch	0.93	57.85	340	IoT, sensing
Gypsum-design	2.4	Silver nanoparticle	PET	Inkjet printing	28 × 35	CPW patch	1.83	66.70	365	IoT, sensing
Plywood-design	2.4	Silver nanoparticle	PET	Inkjet printing	30 × 37	CPW patch	1.00	52.45	425	IoT, sensing

Table 2. A comparison of the proposed antenna arrays with other flexible antenna arrays.

Reference	Freq. (GHz)	Material			Antenna array							MIMO performance				Application
		Conductive	Dielectric	Construction	Size (mm²)	Topology	Gain (dBi)	Efficiency (%)	BW (MHz)	Return loss (dB)	Isolation (dB)	ECC	DG (dB)	MEG (dB)	CCL (bits/s/Hz)	
[22]	1.83–8	Copper	Textile	Custom	70 × 40	1 × 2 Custom	4.4	N/A	Ultra-wide	N/A	>22	<0.01	>9.6	< − 2.53	<0.2	Wearable IoT
[23]	4	Graphene	Kapton	Inkjet printing	62.5 × 72	1 × 4 phased array	8.77	47.7	N/A	N/A	N/A	N/A	N/A	N/A	N/A	Beamforming
[24]	25.6	Silver Ink	PET	Inkjet printing	29.5 × 24.7	1 × 2 Microstrip patch	N/A	N/A	N/A	N/A	N/A	N/A	N/A	N/A	N/A	5G NR
[25]	2.4–2.48	PCPTF	Felt	Glue	124 × 113	2 × 2 Microstrip patch	8.2	56	80	12.6	N/A	N/A	N/A	N/A	N/A	WiFi
[26]	5.8	Conductive fabric	E-glass fiber	Laminating	N/A	1 × 4 Microstrip patch	11.9	75	89	N/A	N/A	N/A	N/A	N/A	N/A	5G NR
[27]	1.83–13.82	Copper	Textile	Custom	50 × 35	1 × 2 Custom	4.21	N/A	Ultra-wide	N/A	>21	<0.059	>9.9	< − 3	<0.35	Wearable IoT
[28]	2–14	Copper	Polyethylene foam	Printing	92 × 92	4-element custom	7.2	N/A	Ultra-wide	N/A	>15	<0.36	>9.6	N/A	<0.4	Wearable IoT
Air-design	2.4	Silver nanoparticle	PET	Inkjet printing	235 × 59	1 × 4 CPW patch	6.54	59.43	340	>17	>22	<0.001	>9.95	< − 3	<0.4	IoT, MIMO
Gypsum-design	2.4	Silver nanoparticle	PET	Inkjet printing	230 × 52	1 × 4 CPW patch	7.06	58.34	365	>16	>21	<0.001	>9.95	< − 3	<0.4	IoT, MIMO
Plywood-design	2.4	Silver nanoparticle	PET	Inkjet printing	232 × 54	1 × 4 CPW patch	6.13	52.62	425	>15	>21	<0.001	>9.95	< − 3	<0.4	IoT, MIMO

2. Antenna structure and fabrication

2.1. Substrate characterization

The primary characteristic of the substrate that affects the design of the printed antenna is its relative permittivity ε_r, which can vary depending on the environment and measurement method. For instance, Mitsubishi NB-TP-3GU100 transparent PET, which was also used as the substrate in the present study, was measured to have ε_r of 6.7 in [34] while ε_r of 2.4 was determined for the same substrate in [35]. Therefore, the permittivity for the present case was obtained through our methods of fabrication.

The dielectric permittivity of the PET substrate was estimated using the differential phase length method [36]. By means of this method, two transmission lines of different lengths were fabricated on the substrate and then measured for their phase response as a function of frequency. The effective permittivity ε_e, valid for the line geometry, can be expressed as

$$\varepsilon_e = \left(\frac{\Delta\phi\, c_0}{2\pi f \Delta L} \right)^2, \qquad (1)$$

where $\Delta\phi$ is the difference between the unwrapped phase responses of the lines, c_0 is the speed of light in vacuum, f is the frequency and ΔL is length difference of the lines. The relationship between ε_e and the substrate's relative permittivity ε_r depends on the exact geometry of the line. This can be determined by using an EM simulation of the line geometry and trying different values for ε_r until the ε_e matches the value from measurement.

In the present case, CPW transmission lines of 190 mm and 63.3 mm length were fabricated on the PET substrate with a similar geometry as the feed line to the printed antenna. A measurement probe consisting of a subminiature version A (SMA) connector with soldered pogo pins was attached to an adjustable micrometer platform that connects the ends of the transmission line to a vector network analyser (VNA) to measure the phase response. The substrate was supported by a 3D-printed platform ensuring that the immediate environment above and below the line was air.

Using the measured phase responses, an average value for the effective permittivity between 2 and 6 GHz was calculated as 1.38. The substrate's relative permittivity was estimated to be 4.8 by entering the line geometry into the Keysight ADS LineCalc programme and iterating until the simulated ε_e matched the value based on the measurement.

In principle, the effect of the measurement probe is present in both of the phase responses. Thus, it is cancelled out because only the phase difference $\Delta\phi$ is considered along with the length difference ΔL. However, in practice, some uncertainty still remains due to the positioning between the measurement probe and the line. By using formulations provided by [36], the

normalized error was calculated with a total ± 1 mm error in the positioning of the probes, which resulted in an error of approximately $\pm 3\%$ for the measurement of ε_e. As this error propagated through the iterative process of finding ε_r, the resulting range of ε_r was determined to be between 4.3 and 5.2. As observed, the error in ε_r was considerably larger than in ε_e. This difference can be explained by an extremely thin substrate that causes the permittivity of air to dominate the ε_e of the line. Thus, a larger change in ε_r was required to affect a smaller change in ε_e. While this causes difficulties in measuring ε_r accurately, it also confers an advantage for coplanar structures on thin substrates. Any deviations in ε_r have relatively less effect on the RF performance with such structures than with thicker substrates or other geometries where the EM fields are more concentrated on the substrate itself, e.g., microstrips.

2.2. Design

The CPW patch antenna is designed to function at 2.4 GHz resonance frequency with bandwidth of over 100 MHz for at least 10 dB return loss. In order to create an initial patch antenna design, the transmission line model of the analytical method [37, 38] is used to roughly calculate the rectangular patch width and length of the antenna. The width W and length L of the patch are expressed by

$$W = \frac{c_0}{2f}\sqrt{\frac{2}{\varepsilon_r + 1}}, \qquad (2)$$

$$L = \frac{c_0}{2f\sqrt{\varepsilon_e}}, \qquad (3)$$

where c_0 is the speed of light and f is the antenna operation frequency. The relative permittivity, which is also called the dielectric constant of the substrate, is denoted by ε_r. The effective permittivity is denoted by ε_e. The relative and effective permittivity values of the substrate were estimated to be 4.84 and 1.38, respectively. This design was iteratively simulated by fine-tuning the antenna dimensions to fulfill the requirement of a 2.4 GHz resonance frequency with a 100 MHz bandwidth of less than -10 dB. Eventually, antenna dimensions were clarified, and the final design was fabricated (please, see the design and fabrication flowchart described in figure 1).

The CPW feed line, as shown in figure 2(a), was dimensioned based on fitting it to a standard PCB edge SMA connector without special consideration given to its transmission line characteristics. The impedance was calculated using the Keysight ADS LineCalc programme at approximately 100 ohms. However, as the feed line has a short length of less than $\lambda/10$, the effect of the apparent impedance mismatch on either the antenna or a nominal 50 ohm system is negligible.

To investigate whether the patch antenna can also fulfill the same requirements as being attached
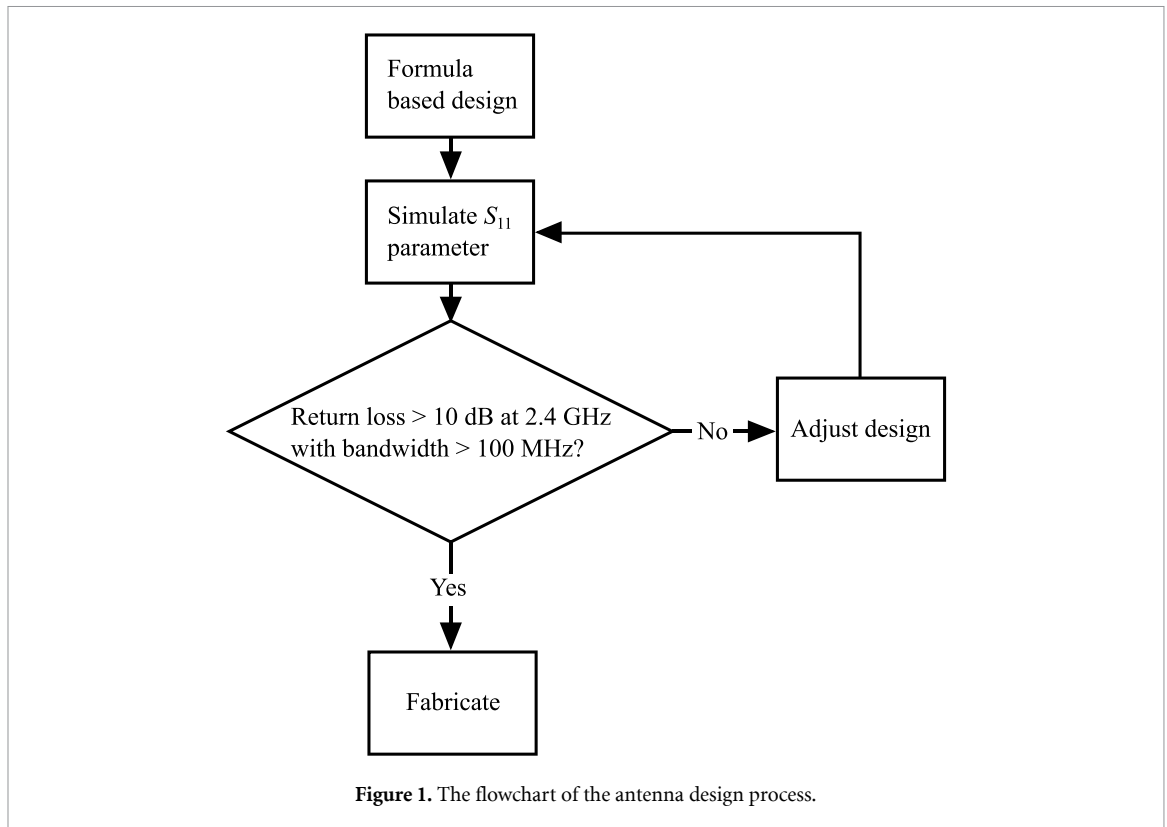
Figure 1. The flowchart of the antenna design process.

Part	Value (mm)
a	10.0
g	6.0
a_pin	3.0
g_pin	6.0
d	1.0
d_pin	1.2
L	42.0
W	34.0

(a)

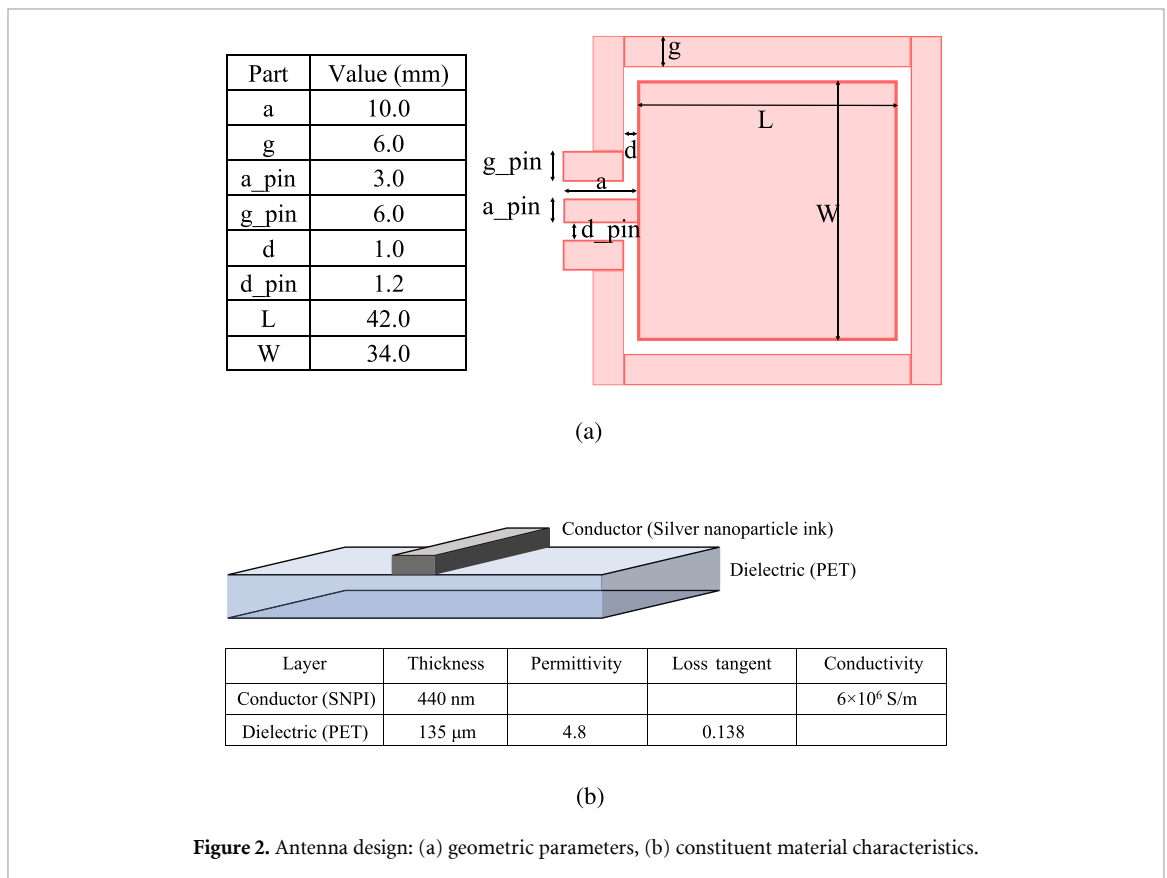| Layer	Thickness	Permittivity	Loss tangent	Conductivity
Conductor (SNPI)	440 nm			6×10^6 S/m
Dielectric (PET)	135 μm	4.8	0.138	

(b)

Figure 2. Antenna design: (a) geometric parameters, (b) constituent material characteristics.

to different background materials, additional investigations with the plywood board and the gypsum board were conducted. The main driver for the selection of these materials was their prevalence in the construction of indoor walls. Since these materials have higher permittivity than air, they are generally expected to affect the resonance frequency and the radiation pattern of the antenna. The S_{11}
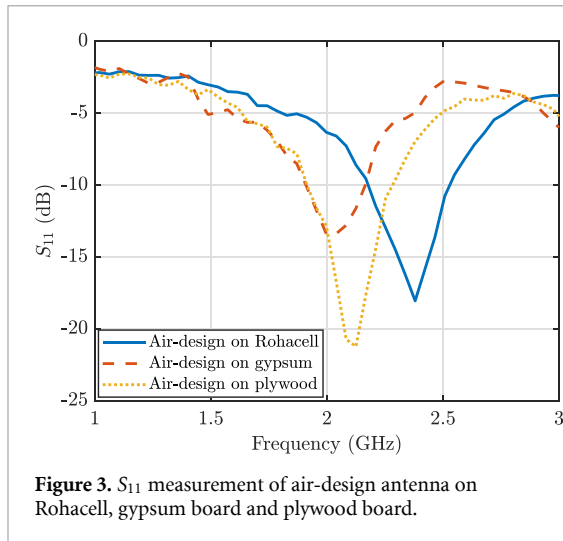
Figure 3. S_{11} measurement of air-design antenna on Rohacell, gypsum board and plywood board.

Table 3. Antenna dimensions.

Material	L (mm)	W (mm)	f_{bg} (GHz)
Air-design	42	34	2.4
Gypsum-design	35	28	2.0
Plywood-design	37	30	2.1

measurements shown in figure 3 verified this expectation. To compensate for the changes in resonance frequencies caused by the gypsum and plywood, two new antenna designs were created. These gypsum and plywood designs are re-scaled versions of the original air-design, with provided dimensions in table 3. The new dimensions for the re-scaled patch antenna design can be expressed by rough estimation

$$x_{bg} \approx \frac{f_{bg}}{f_{air}} \cdot x_{air}, \qquad (4)$$

where f_{bg} is the measured resonance frequency dip with some background material and f_{air} is the measured resonance frequency, with air surrounding the antenna. Variable x_{air} is the original size of the patch antenna width or length. In this case, f_{air} is 2.4 GHz since it is the targeted frequency of the air-design.

In addition to single antenna designs, antenna arrays were another design objective of the present investigations. To construct a highly directive array, the antennas were fabricated in rows of four. An empirical half-wavelength ($\lambda/2$) spacing between array elements was implemented. This configuration was carried out for the air, gypsum, and plywood designs.

2.3. Fabrication
Mitsubishi NBSIJ-MU01 silver nanoparticle ink (viscosity of 2.30 mPa.s and surface tension of 32 mN m^{-1}) and A4-size Mitsubishi NB-TP-3GU100 PET substrate (microporous Al$_2$O$_3$-*PVA* single-sided coating and sheet thickness of 135 ± 12 µm) was used with low-cost EPSON WF-2840 DWF printer (resolution of 5760×1440 dots per inch) as depicted in

figure 4(a). The microporous coating of the substrate was designed so that the silver nanoparticle ink can be efficiently absorbed and react rapidly, which results in highly conductive layers. Following the printing process, 1500 W photonic curing was applied to the printed surface for 15 s to sinter the ink [8], seen in figure 4(b). It is worth noting that the photonic curing is a local process, which effectively reduces the thermal stresses over the substrate, hence warping and degradation, and curing time when compared with the convective oven sintering occurring at high temperatures [39].

A complete A-4 sheet of inkjet-printed antennas is shown in figure 5(a). By means of a novel yet extremely low-cost and non-abrasive in-house 3D printed polylactic acid (PLA) tightener, as designed and demonstrated in figure 5(b), SMA connectors were modularly plugged into these antennas, shown in figure 5(c). Hence, the use of soldering or conductive epoxy paste was totally eliminated.

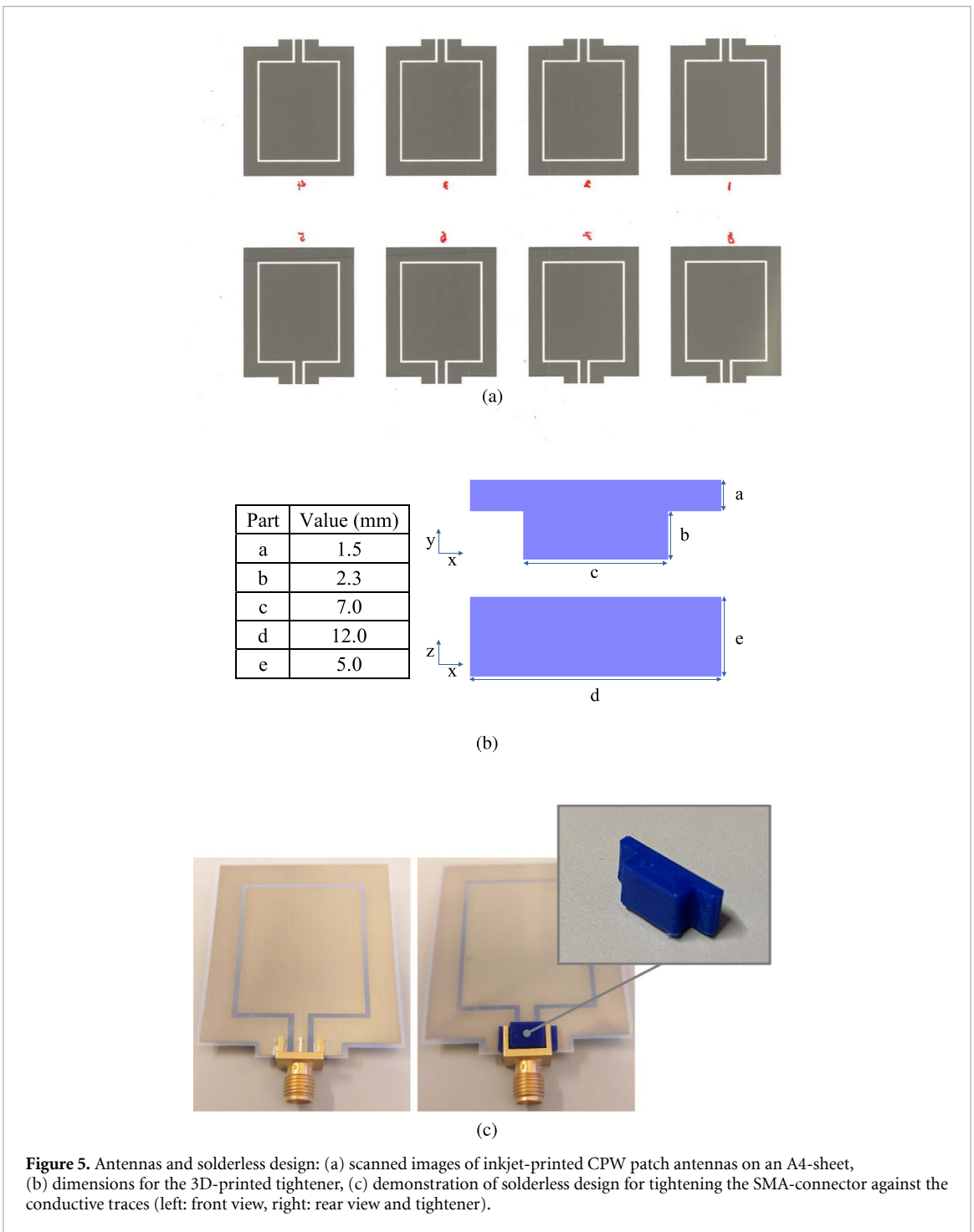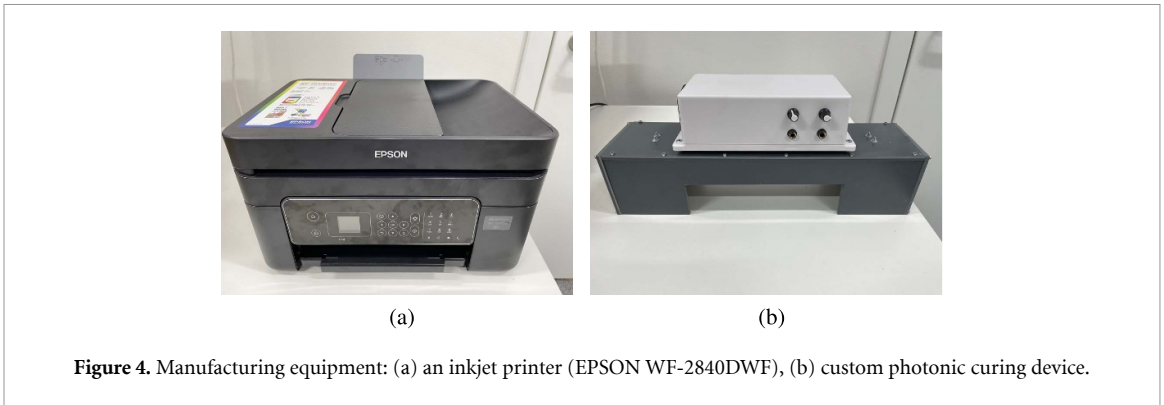## 3. Antenna simulation and optimization

3.1. Simulations
The antenna return loss (S_{11} parameter) and far-field radiation pattern simulations were carried out before printing to investigate whether the CPW patch antenna designs had the potential to fulfill the aforementioned requirements. Keysight Advanced Design System (ADS) 2022 Update 1 was selected as the software for running the simulations, which integrates several simulation methods, e.g., Momentum (RF), Momentum (microwave) and the finite element method, for antenna layouts. The details of these methods can be found in the software documentation [40]. In the present investigations, the Momentum (microwave) method was selected as the solver over the antenna solution domain depicted in figure 6.
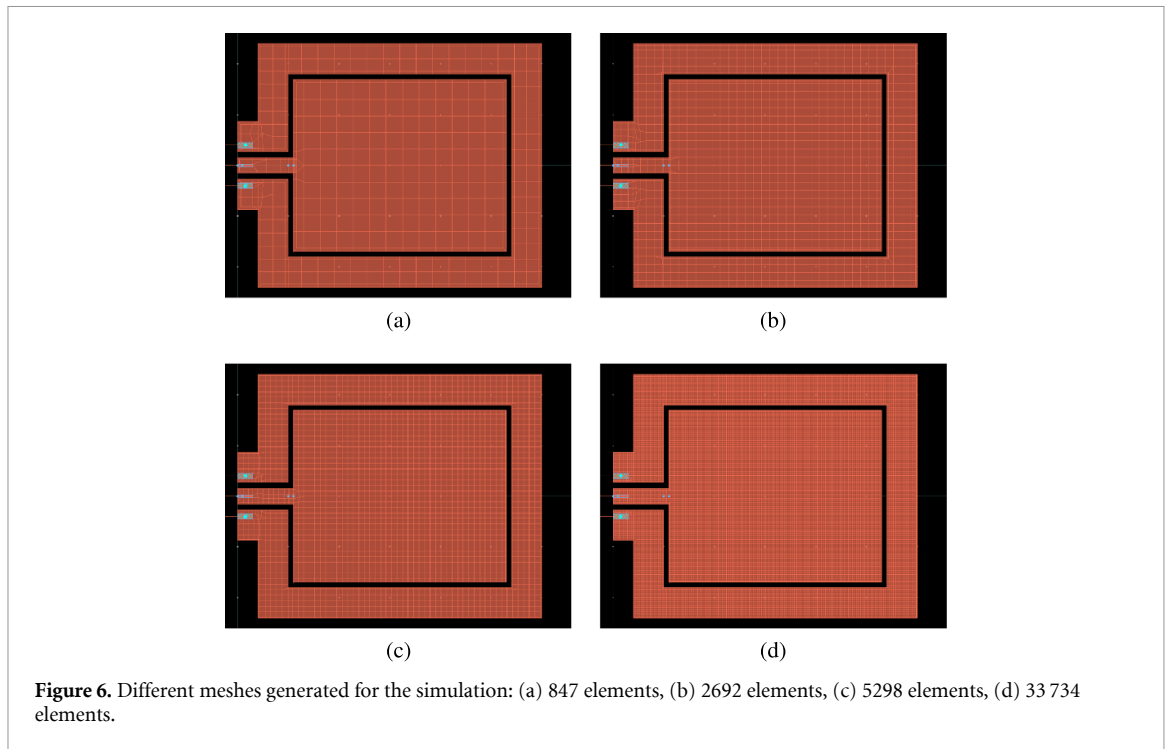
In the first stage, a mesh convergence study was carried out to determine the optimal number of elements to be used for the simulations with reliable results and reasonable computational times. Thereafter, the single antenna and antenna array simulations were carried out to investigate whether the design requirements were achieved.

For the solution domain, a substrate model was defined as a dielectric medium based on the Mitsubishi NB-TP-3GU100 characteristics, on top of which the conductive layer was appended by using the Mitsubishi NBSIJ-MU01 silver nanoparticle ink characteristics as listed in figure 2(b). The rest of the material surrounding the substrate is assumed to be air. Further details are also tabulated in figure 2(b).

3.2. Mesh convergence study
A mesh convergence study was carried out to determine the optimal number of elements for numerical analysis. Some of the layout meshes generated for the
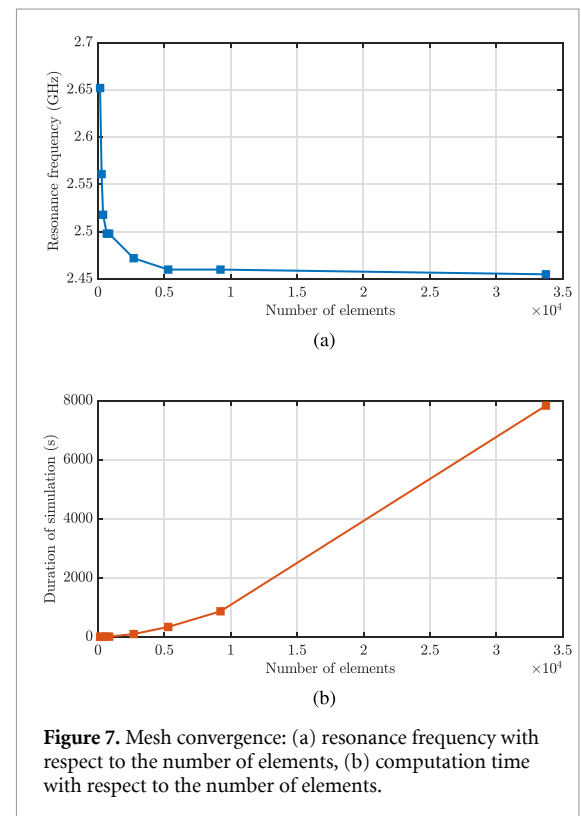
Figure 4. Manufacturing equipment: (a) an inkjet printer (EPSON WF-2840DWF), (b) custom photonic curing device.

Part	Value (mm)
a	1.5
b	2.3
c	7.0
d	12.0
e	5.0

Figure 5. Antennas and solderless design: (a) scanned images of inkjet-printed CPW patch antennas on an A4-sheet,
(b) dimensions for the 3D-printed tightener, (c) demonstration of solderless design for tightening the SMA-connector against the conductive traces (left: front view, right: rear view and tightener).

Figure 6. Different meshes generated for the simulation: (a) 847 elements, (b) 2692 elements, (c) 5298 elements, (d) 33 734 elements.

study are shown in figure 6. In the ADS momentum (microwave) simulations, the 'cells/wavelength' parameter was fine-tuned to control the number of elements in the solution domain, thus the distance to the lowest wavelength in the simulated frequency range was estimated. Thereafter, the convergence simulations were carried out by sweeping the frequency within the range from 0 to 8 GHz with 240 points. Frequencies of 2.40 GHz, 2.41 GHz, 2.45 GHz and 2.46 GHz were intentionally inserted due to them being within the investigated frequency ranges for the present indoor applications. As the solution domain started to have a finer mesh, the resonance frequency measured with S_{11} settled around the 2.46 GHz region. As plotted in figure 7(a), this behaviour was observed to become stable with the number of elements greater than 5000. On the other hand, the computational time was deduced to increase with the increasing number of elements as shown in figure 7(b). Therefore, to obtain reliable outcomes within a reasonable duration, the solution domain with 5298 elements for a single antenna was used for further numerical analysis in the present study.

Figure 7. Mesh convergence: (a) resonance frequency with respect to the number of elements, (b) computation time with respect to the number of elements.

3.3. Single antenna and antenna array simulations

The CPW patch antenna designs were simulated with ADS. The first configuration contains a patch antenna air-design. The second configuration contains four patch antennas organized in an array configuration. Both simulations were run with the substrate parameters described by 2(b).

Two simulation scenarios were generated: a single antenna at 1.0–3.0 GHz with 41 linearly spaced frequency points, and an antenna array at 1.0–3.0 GHz with 41 linearly spaced frequency points. These frequency ranges were selected to determine the antenna characteristics at and near the resonance frequency. A mesh frequency of 80 cells per wavelength was used with 5000 elements as previously described in the mesh sensitivity study.

4. Antenna measurement and characterization

To validate and assess the antenna design, both the printed antennas and the antenna arrays were characterized in terms of *S*-parameters and far-field radiation pattern. A Rhode & Schwarz VNA ZNB 8 was used to investigate the *S*-parameters of the antennas, and the StarLab antenna measurement system[2] was used to measure the radiation pattern of the antenna and the antenna array, shown in figure 8(b). The antenna under test (AUT) received the EM waves transmitted by the measurement antennas circularly embedded in the StarLab anechoic chamber and then fed the receiving port of the chamber. The measurement antennas of the chamber were connected to the Port 1 (transmitting port) of a VNA Keysight E5071C ENA, and the AUT was connected to the Port 2 (receiving port) of the same VNA through the feeding port of the chamber. If the AUT is a proposed four-element antenna array, a four-way power combiner is used to feed the Port 2 of VNA with total received power from all four elements. A host PC was utilized to control the radiation of the measurement antennas and to collect measurement data from the VNA. The output data were further processed by MATLAB to generate radiation pattern plots of the AUT. Using such a measurement system, the scattering parameter S_{21} of the AUT can be measured from various directions of the measurement antennas, resulting in a complete AUT characterization in a 3D space. In sequel, measurement results for both the antennas and antenna arrays are shown and discussed. Furthermore, as a potential enabler for MIMO communications, the antenna array diversity performance was evaluated based on *S*-parameters measurement results.

4.1. Single antenna

As a first step, the simulated and measured S_{11} values for a single air-design antenna were compared, shown in figure 9. The simulation curve was determined to have a dip of -16.81 dB at 2.47 GHz, while the measurement curve had a dip of -18.05 dB at 2.38 GHz. For a clear comparison, the S_{11} measurements of the single gypsum-design antenna attached to the gypsum board, as well as the single plywood-design antenna attached to the plywood board are also depicted in figure 9. The S_{11} curve of the gypsum-design had a dip of -19.61 dB at 2.47 GHz, and the curve of the plywood design had a dip of -25.72 dB at 2.42 GHz. There were shifts of a few tens of megahertz due to the SMA connector introducing a static capacitance and increasing the electrical length of the

device. The dips presented around 2.4 GHz indicate that the printed antenna can be well operated in the desired frequency band. The range of frequencies for the return loss higher than 10 dB was around the range between 2.2 GHz and 2.5 GHz, which provides beyond 300 MHz operational bandwidth of all antennas. In order to characterize the proposed antenna designs as being attached to their corresponding background materials shown in figure 8(a), the radiation patterns of the three antenna designs were investigated in the following sections.
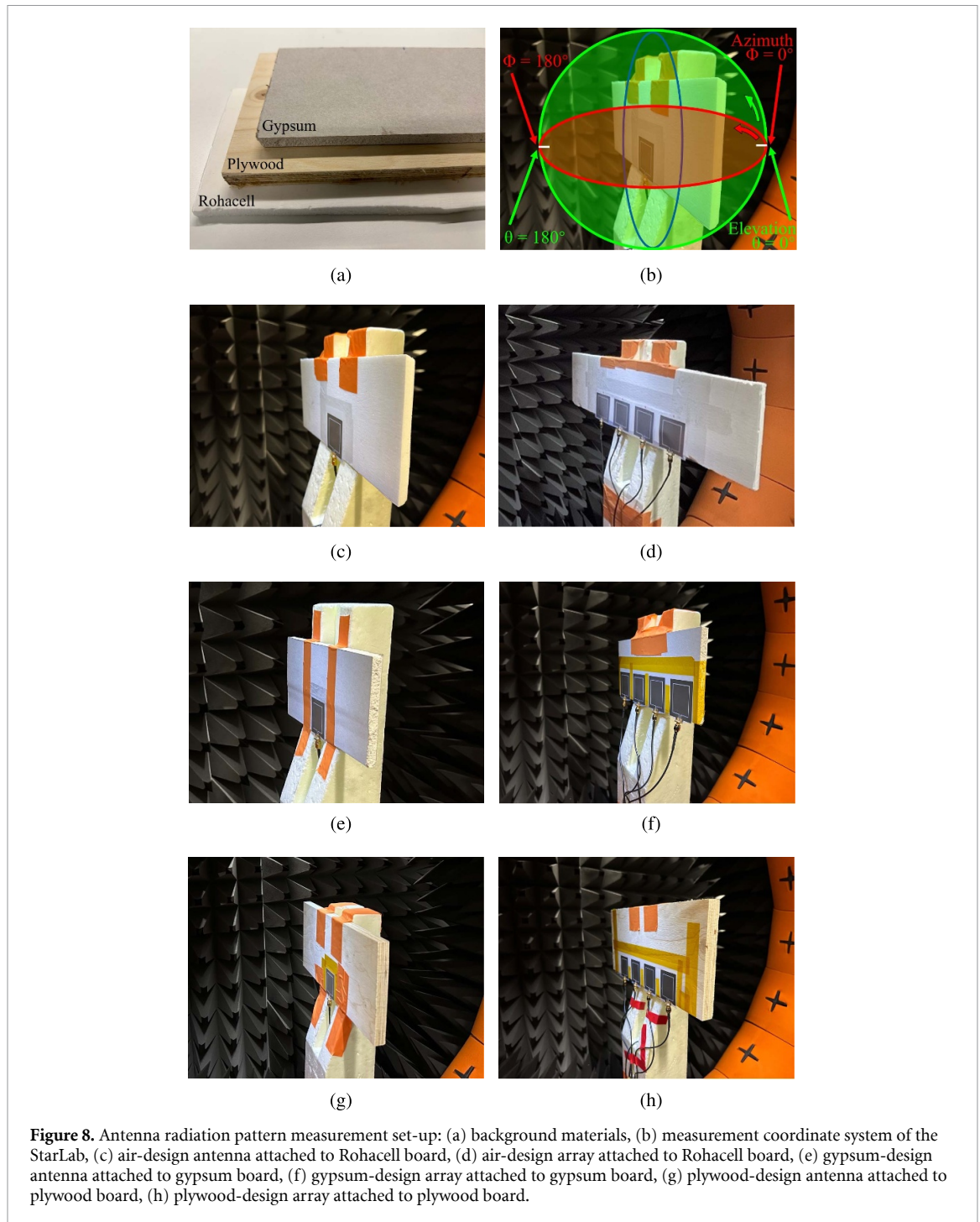
4.1.1. The air-design antenna

As a benchmark, the radiation pattern of the air-design antenna was simulated and measured. As seen in figure 8(c), the antenna-attached Rohacell is a common holder or standing material in antenna characterization with negligible effect on the radiation pattern. As measured and also illustrated in figures 10(a) and (b), the measured 3D radiation pattern was in agreement with the simulated one. In figures 10(c) and (d), the 2D pattern polar plots of both azimuth cut (E-plane) and elevation cut (H-plane) were displayed for both simulation and measurement. The simulated antenna peak gain (1.39 dBi) and the measured one (0.93 dBi) also show a good agreement with the measured half power beam width (HPBW) existing around 144°.

It was further noticed that the antenna simulations demonstrated an ideal coplanar patch antenna, for which the antenna did not radiate towards angles coplanar to the antenna. These angles were plotted as gaps in the simulated radiation patterns. Such angles in this case refer to the azimuth and elevation angles of 90° and 270°, respectively. Apparently, the radiation pattern measured in Starlab did not exhibit the same behaviour at these angles since the set-up did not measure the AUT at exactly the same angles.

4.1.2. The gypsum-design antenna

The gypsum-designed antenna was fabricated and attached to a gypsum board to measure its radiation pattern, as shown in figure 8(e). For proper comparison, the air-design antenna was also attached to the same gypsum board, and the radiation patterns were measured. Figures 11(a) and (b) indicate that the air-design antenna and gypsum-design antenna have similar shapes of 3D radiation patterns. However, once the cutting plots shown in figures 11(c) and (d) were examined, clear differences exist in the antenna gain over 3 dBi, for which the gypsum-design has a peak gain of 1.83 dBi while the air-design has only a peak gain of -1.78 dBi. Thus, it was proven that the proposed gypsum-designed antenna could radiate or receive more energy than the air-design antenna that was also attached to the same gypsum board and subjected to the same ambient conditions.

Figure 8. Antenna radiation pattern measurement set-up: (a) background materials, (b) measurement coordinate system of the StarLab, (c) air-design antenna attached to Rohacell board, (d) air-design array attached to Rohacell board, (e) gypsum-design antenna attached to gypsum board, (f) gypsum-design array attached to gypsum board, (g) plywood-design antenna attached to plywood board, (h) plywood-design array attached to plywood board.

4.1.3. The plywood-design antenna

As seen in figure 8(g), the plywood-design antenna was also attached to the plywood board so as to measure the radiation pattern. For comparison purposes, the same procedure as in the gypsum case was implemented, i.e. in the air-design antenna was attached to the same plywood board to measure and compare its radiation pattern with the one for the plywood-design antenna. In figures 12(a) and (b), the air-design antenna and plywood-design antenna can be seen to have similar shapes of 3D radiation patterns. Similar to the gypsum case, their cutting plots were also demonstrated to have clear differences

in antenna gain around 3 dBi, where the plywood-design has a peak gain of 1.00 dBi while the air-design has only a peak gain of -1.79 dBi (please, see figures 12(c) and (d)). Thus, the proposed plywood-design antenna is determined to radiate or receive more energy than the air-design antenna under the same conditions as the same plywood board.

For the azimuth cuts shown in figures 11(c) and 12(c), there existed a shift of radiation towards 90° and 270° angles, which was assumed to be caused by the attached background materials (here, gypsum and plywood boards). Both materials have higher relative permittivity than the air surrounding the AUT

Figure 9. S_{11} simulations and measurements for antennas as being attached to the corresponding materials.

Figure 10. Radiation pattern of a single antenna at 2.4 GHz (Unit: dBi): (a) simulation of 3D radiation pattern, (b) measurement of 3D radiation pattern, (c) azimuth cut, (d) elevation cut.
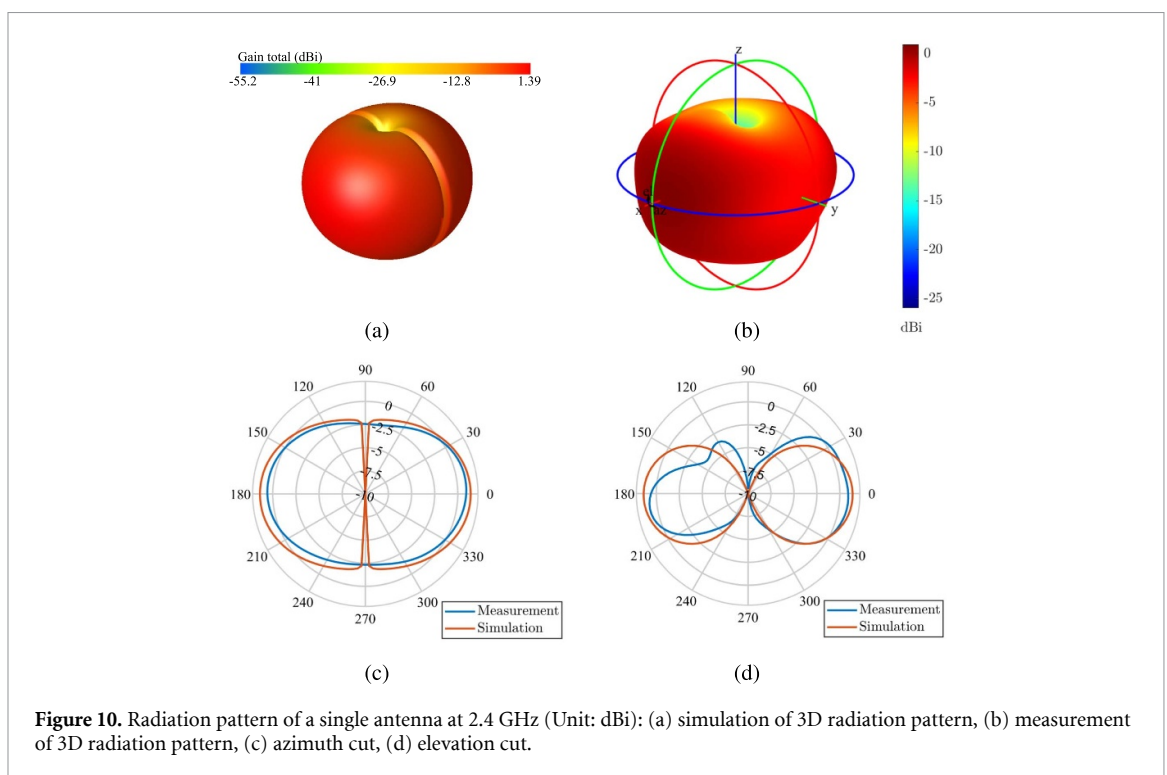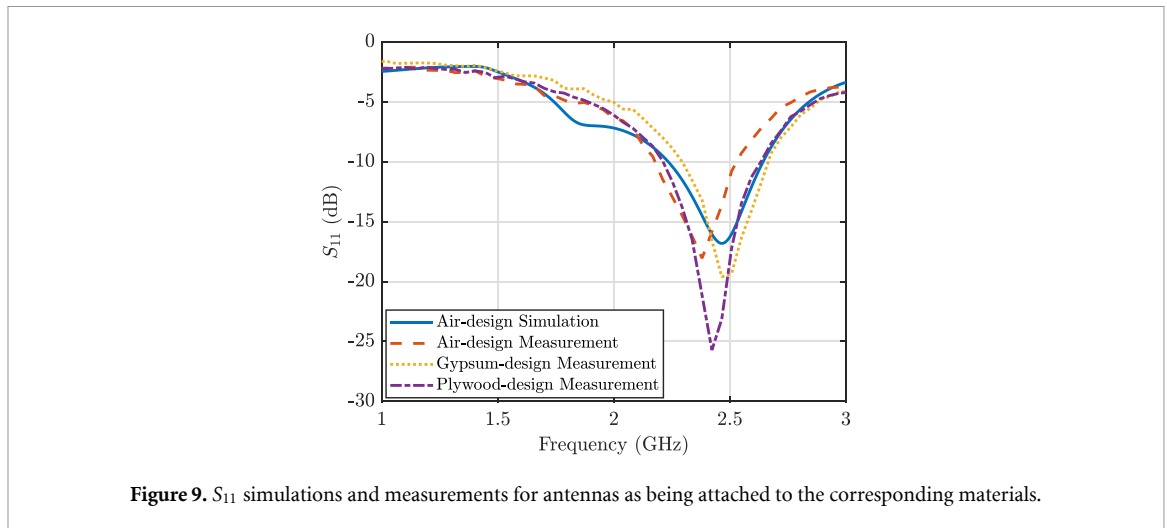
in other directions. This shift is troublesome if we expect the antennas to radiate or receive more power from the direction of 180°, opposite to the attached materials. In the following section, antenna arrays that are capable of compensating such issues with higher gains for both directions of 0° and 180° will be introduced.

In addition, the efficiency of each antenna attached to its corresponding material is shown in figure 13(a). All the measured antenna efficiencies were above 50% around 2.42 GHz. For the air-design antenna, the difference between the simulated and measured efficiencies might be induced by multiple factors, e.g., the connection between the SMA connector and antenna pins, as well as losses of the substrate at the resonance frequency.

4.2. Antenna array

4.2.1. The air-design antenna array

First, as a benchmark, the radiation pattern of the antenna array composed of four air-design elements was simulated and measured. As seen in figure 8(d), similar to the single air-design antenna measurement, the array is held by a Rohacell board that has a negligible effect on its radiation pattern. In figures 14(a) and (b), the measured 3D radiation pattern can be seen, which is in agreement with the simulation results.

Furthermore, in figures 14(c) and (d), the 2D pattern polar plots of both azimuth cut (E-plane) and elevation cut (H-plane) were also shown for both simulation and measurement. The simulated array peak gain (8.85 dBi) and the measured one (6.54 dBi)
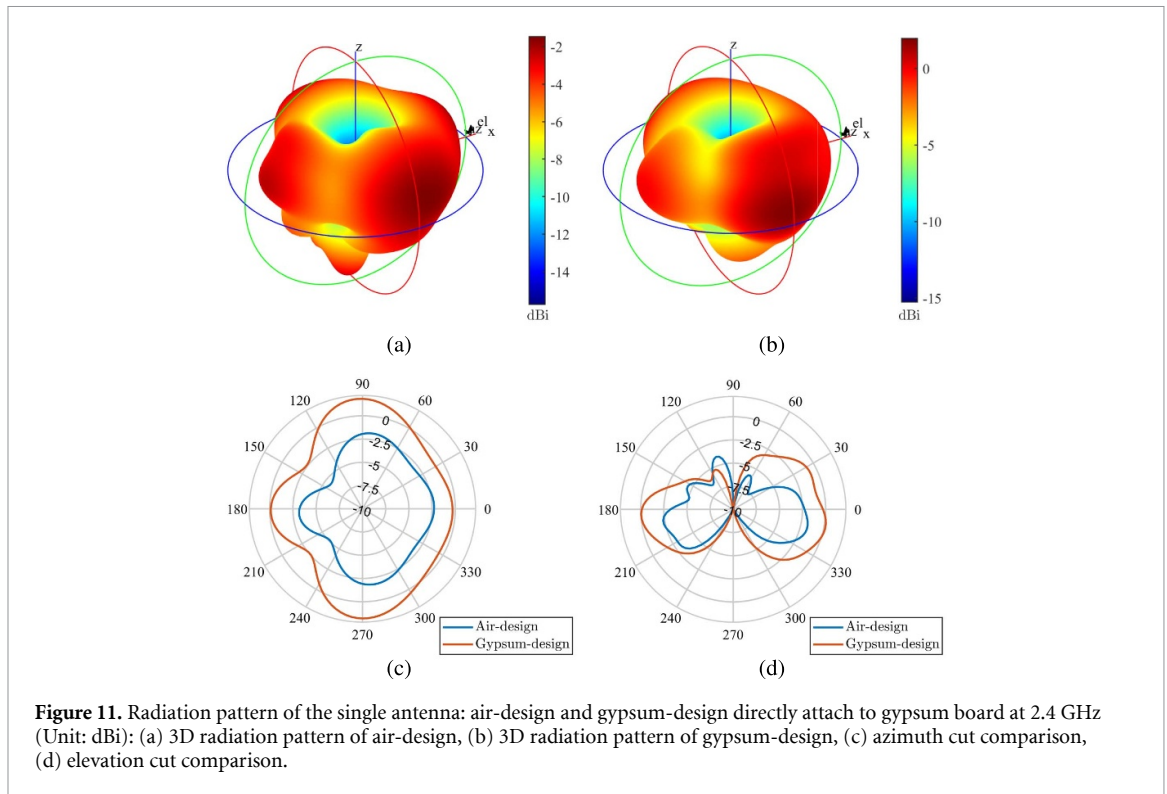
Figure 11. Radiation pattern of the single antenna: air-design and gypsum-design directly attach to gypsum board at 2.4 GHz (Unit: dBi): (a) 3D radiation pattern of air-design, (b) 3D radiation pattern of gypsum-design, (c) azimuth cut comparison, (d) elevation cut comparison.
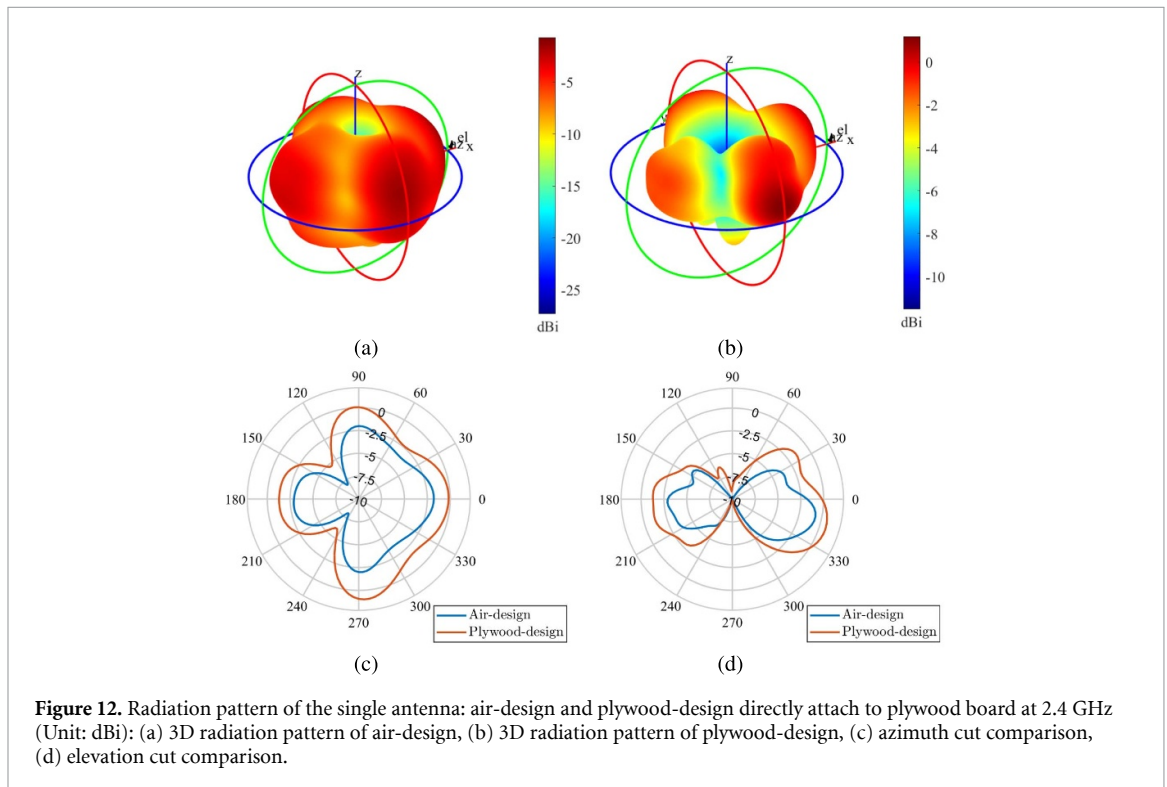
Figure 12. Radiation pattern of the single antenna: air-design and plywood-design directly attach to plywood board at 2.4 GHz (Unit: dBi): (a) 3D radiation pattern of air-design, (b) 3D radiation pattern of plywood-design, (c) azimuth cut comparison, (d) elevation cut comparison.

show an acceptable agreement and the measured HPBW exists around 30°.

4.2.2. The gypsum-design antenna array
After the benchmark investigations on the air-design antenna array, the gypsum-design antenna arrays

were investigated, which were attached to the gypsum board as shown in figure 8(f). Following the present protocol of comparison, the air-designed antenna array was also attached to the same gypsum board, and its radial pattern was simultaneously measured. In figures 15(a) and (b), the air-design array and
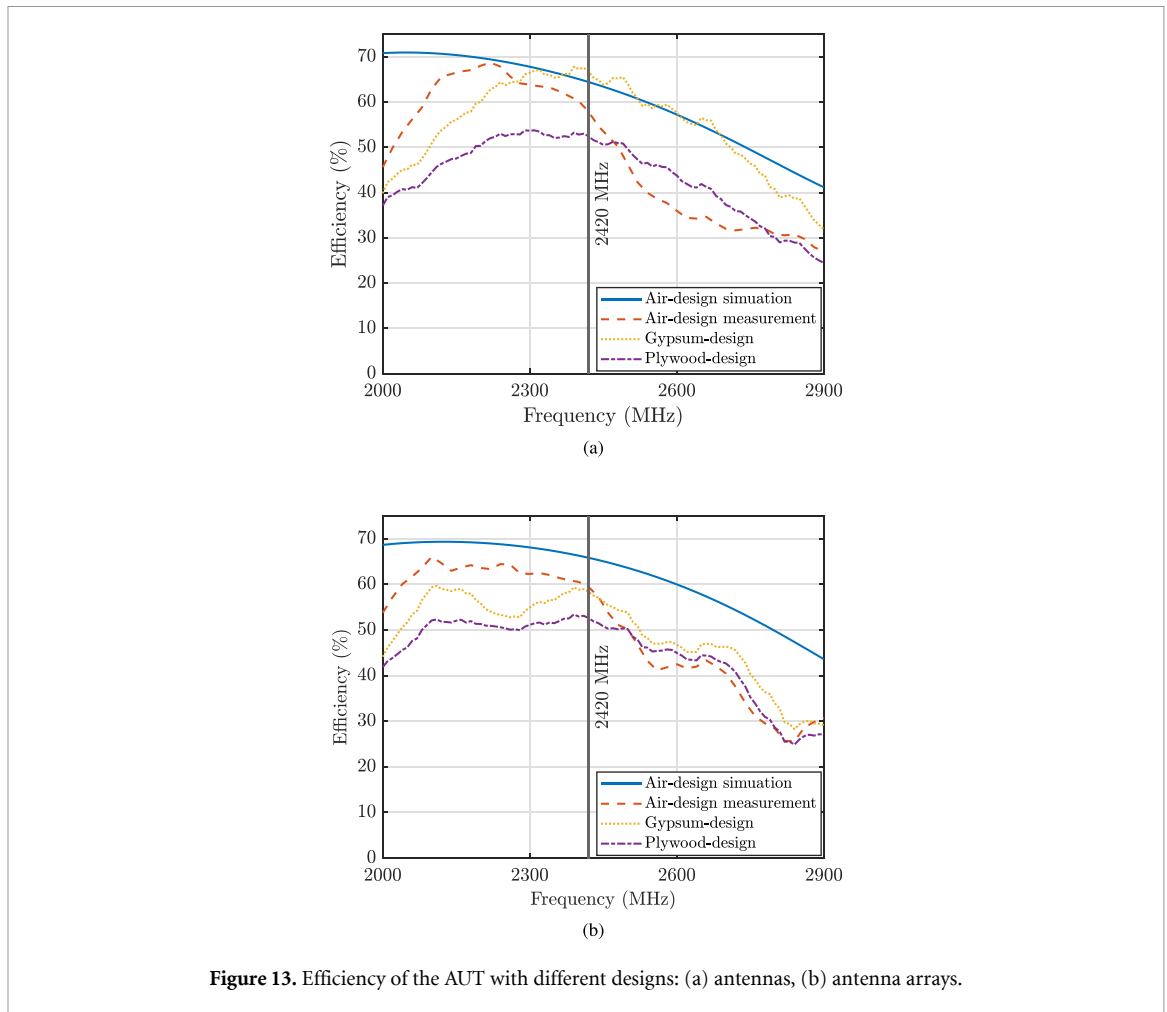
Figure 13. Efficiency of the AUT with different designs: (a) antennas, (b) antenna arrays.
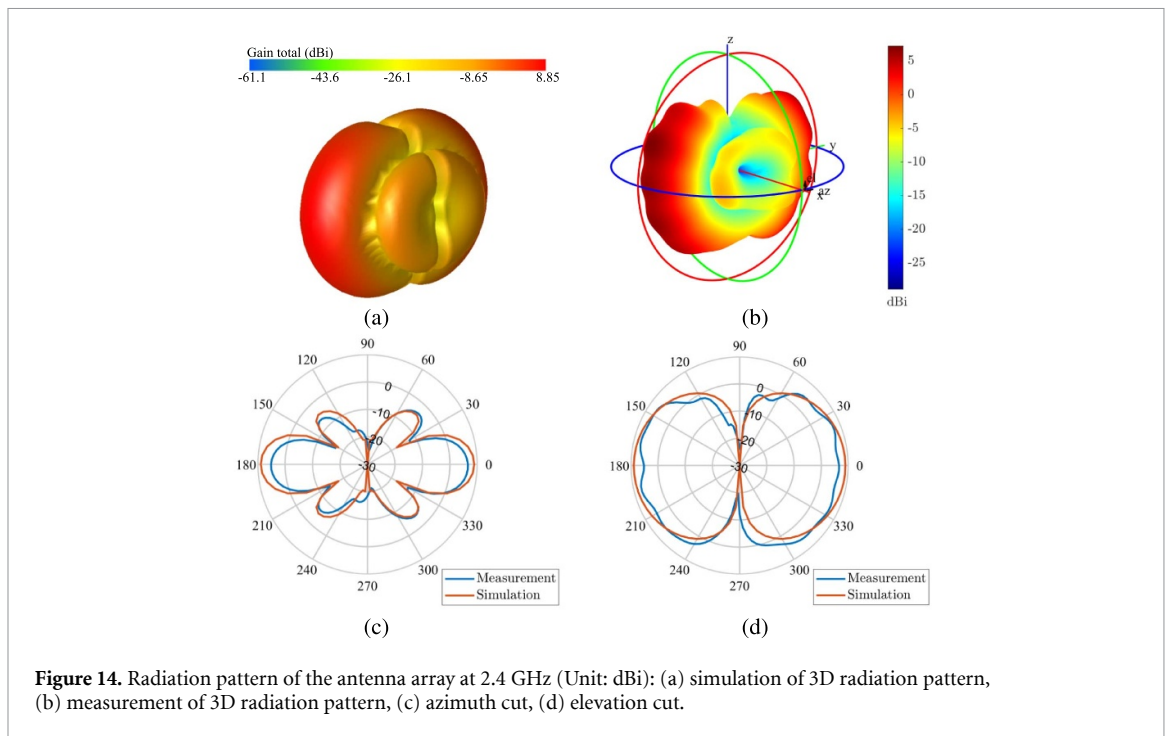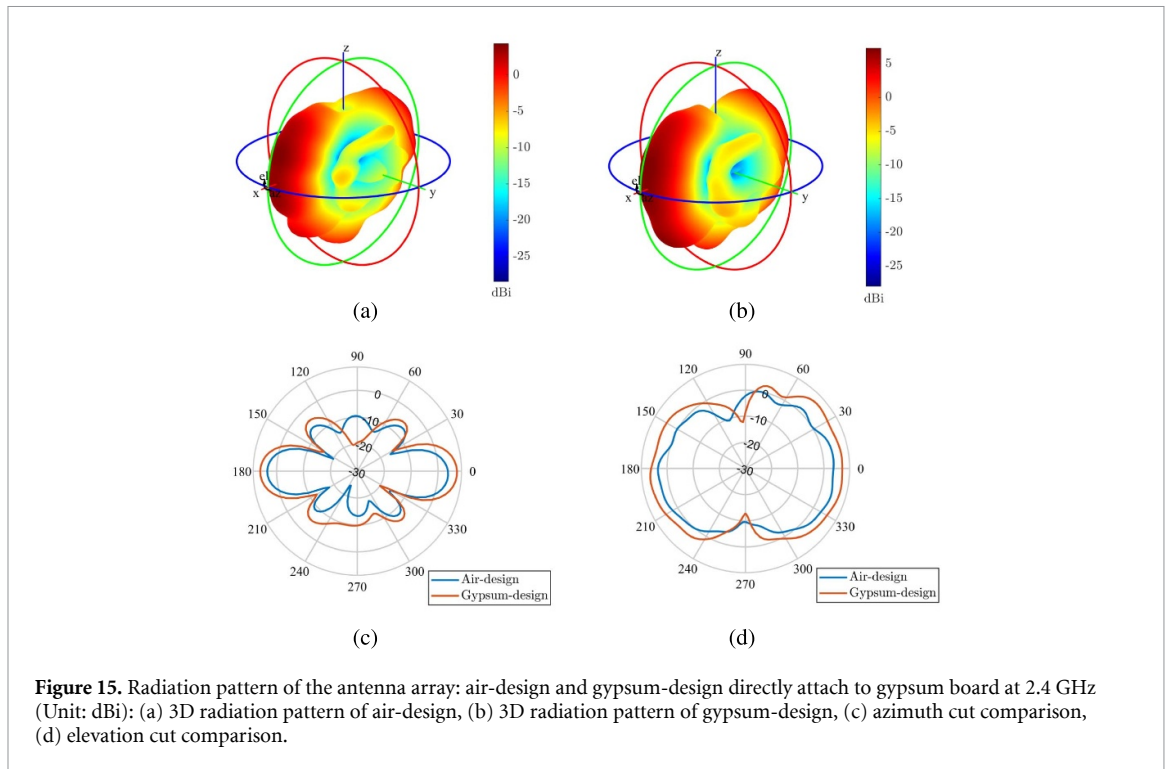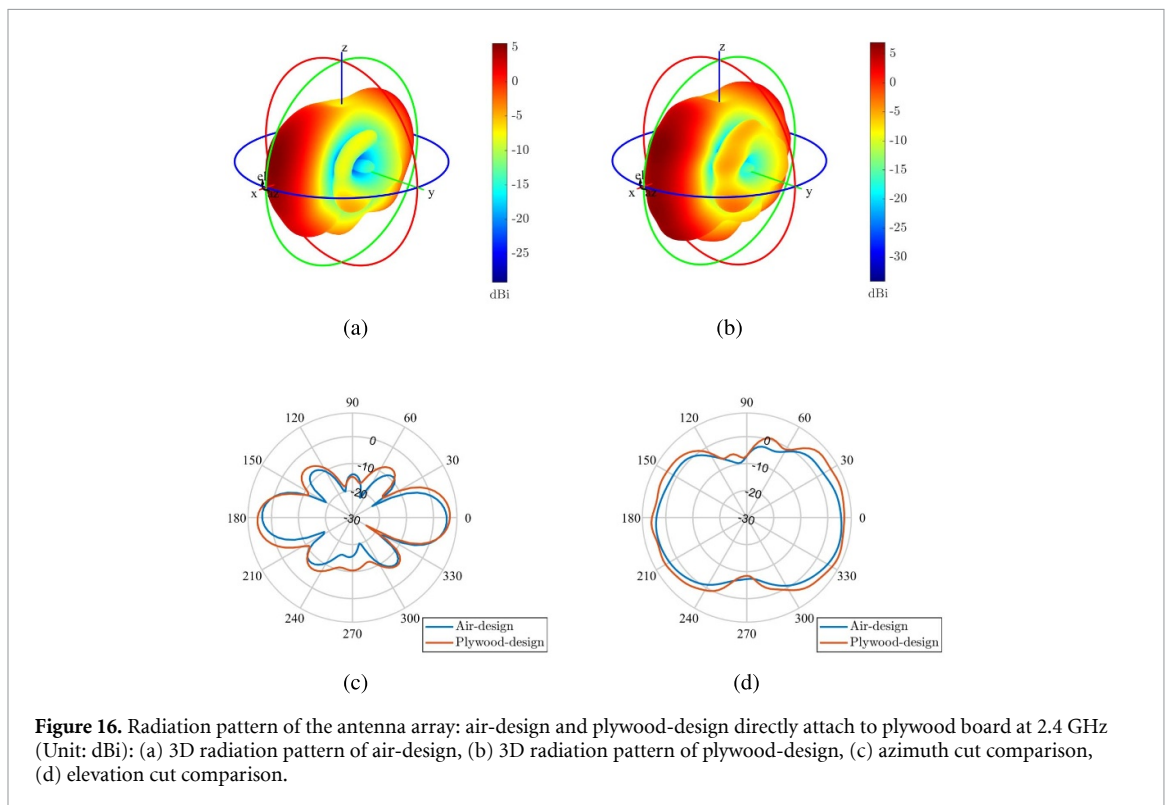

Figure 14. Radiation pattern of the antenna array at 2.4 GHz (Unit: dBi): (a) simulation of 3D radiation pattern, (b) measurement of 3D radiation pattern, (c) azimuth cut, (d) elevation cut.

gypsum-design array were measured to have similar shapes of 3D radiation patterns. Once again, the cutting plots of figures 15(c) and (d) demonstrated

obvious differences in gain over 3 dBi, where the gypsum-design array had a peak gain of 7.06 dBi, while the air-design array had only a peak gain of

Figure 15. Radiation pattern of the antenna array: air-design and gypsum-design directly attach to gypsum board at 2.4 GHz (Unit: dBi): (a) 3D radiation pattern of air-design, (b) 3D radiation pattern of gypsum-design, (c) azimuth cut comparison, (d) elevation cut comparison.


Figure 16. Radiation pattern of the antenna array: air-design and plywood-design directly attach to plywood board at 2.4 GHz (Unit: dBi): (a) 3D radiation pattern of air-design, (b) 3D radiation pattern of plywood-design, (c) azimuth cut comparison, (d) elevation cut comparison.

3.67 dBi. Thus, the proposed gypsum-design array was deduced to radiate or receive more energy than the air-design array with the same gypsum board background and ambient conditions.

4.2.3. The plywood-design antenna array

Following the gypsum-designed antenna array measurements, the investigations were also carried out

on the plywood-designed antenna array attached to the plywood board, the measured radiation pattern of which is shown in figure 8(h). The air-design antenna array was also attached to the same plywood board to measure and compare the radiation pattern with the one for the plywood-design antenna. In figures 16(a) and (b), the 3D radiation patterns for air-design array and plywood-design array were
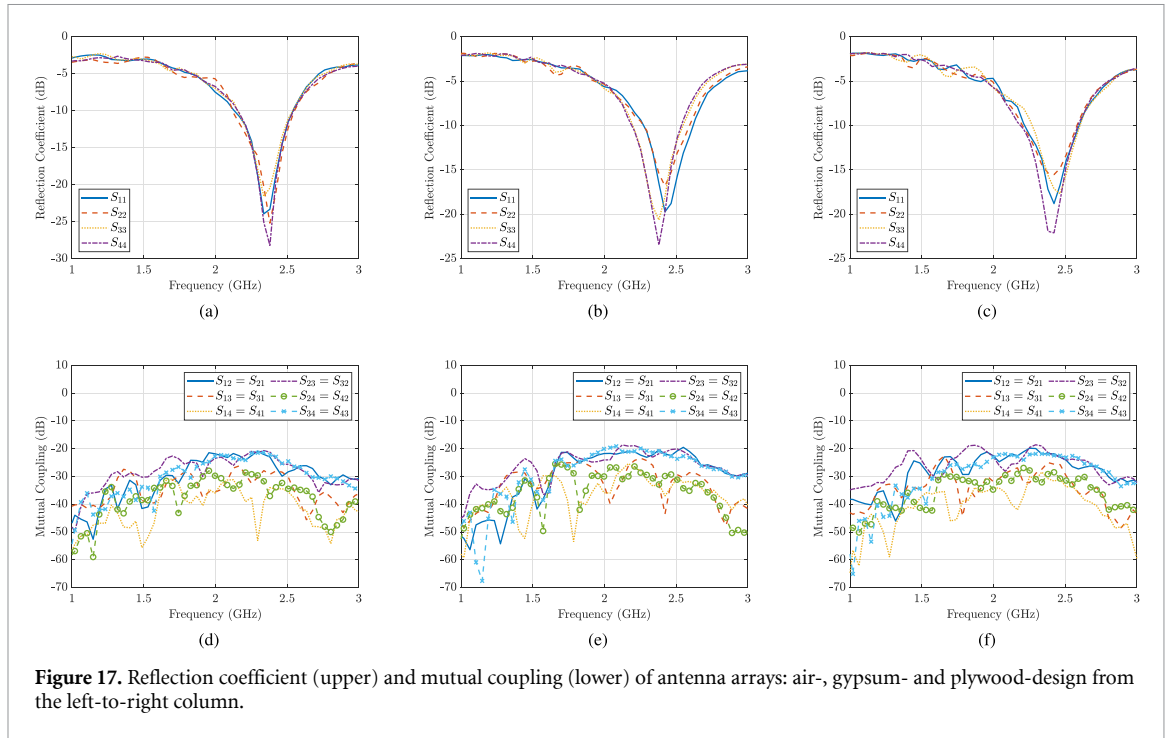
Figure 17. Reflection coefficient (upper) and mutual coupling (lower) of antenna arrays: air-, gypsum- and plywood-design from the left-to-right column.

depicted, which exhibited similar forms. Nevertheless, their cutting plots, as shown in figures 16(c) and (d), demonstrated a difference of gain over 1 dBi, where the plywood design had a peak gain of 6.13 dBi, while the air-design had only a peak gain of 4.97 dBi. This shows that the proposed plywood-designed array can radiate or receive more energy than the air-design array with the same configurations.

For the azimuth cuts shown in figures 15(c) and 16(c), similar to the single antenna cases, it was noticed that there was a shift of the radiation towards the direction of 90° and 270°, which was caused by the attached background materials in such directions. However, for each antenna array, the gains in both directions, 0° and 180°, were measured to be higher than 4 dBi, which supports radiation or receiving more energy as them being attached to the corresponding materials.

The efficiency of each antenna array attached to its corresponding material is shown in figure 13(b). All the measured array efficiencies were above 50% around 2.42 GHz. For the air-design array, the difference between the simulated and measured efficiencies might be induced by similar reasons described previously in section 4.1.

4.3. MIMO antenna diversity performance

The designed antenna arrays introduced in section 4.2 can enable MIMO communication. The diversity performance indicators [41] of the MIMO antenna array system were evaluated in sequels such as return loss (reflection coefficient), isolation (mutual coupling),

envelope correlation coefficient (ECC), diversity gain (DG), mean effective gain (MEG) and channel capacity loss (CCL).

4.3.1. Return loss and isolation

The measured reflection coefficients of the air-, gypsum-, and plywood-designed antenna arrays were shown in figures 17(a)–(c) in their respective order. For the operating frequency band of 2.4 GHz, all four elements of the air-design had return losses beyond 20 dB, and all four elements of the gypsum- and plywood-design had return losses of more than 15 dB. Furthermore, isolation, also known as mutual coupling between individual elements of each array, was investigated, shown in figures 17(d)–(f). For all three arrays, the isolation between the four elements was more than 20 dB.

4.3.2. Envelope correlation coefficient

To further investigate the correlation of radiation patterns between elements of antenna arrays, the ECC can be expressed with *S*-parameters of the array system [42, 43]. The ECC between element *i* and *j* of the *N*-element array is calculated by

$$\rho_e(i,j,N) = \frac{\left| \sum_{n=1}^{N} S_{in}^* S_{nj} \right|^2}{\Pi_{k=\{i,j\}} \left(1 - \sum_{n=1}^{N} S_{in}^* S_{nk} \right)}, \quad (5)$$

where $*$ denotes the complex conjugation. For example, the ECC between the first and second elements of the proposed 4-element array can be expressed by
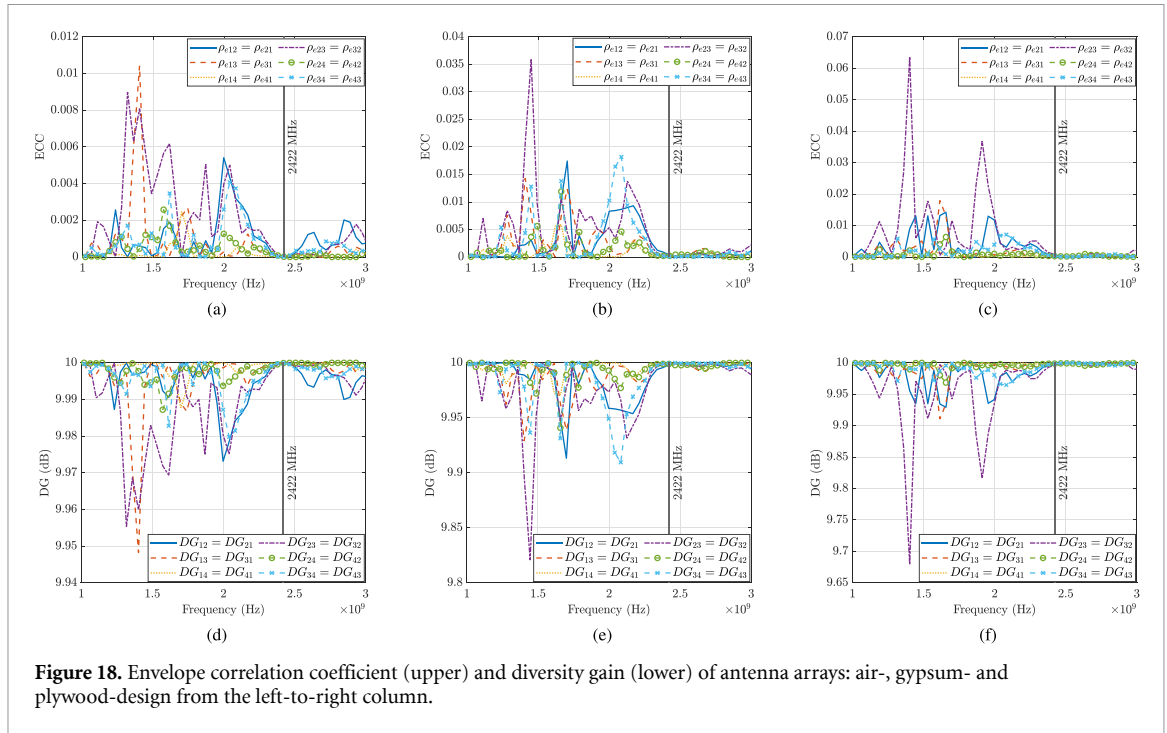
Figure 18. Envelope correlation coefficient (upper) and diversity gain (lower) of antenna arrays: air-, gypsum- and plywood-design from the left-to-right column.

$$\rho_{\mathrm{e}}(1,2,4) = \frac{\left|S_{11}^*S_{12} + S_{12}^*S_{22} + S_{13}^*S_{32} + S_{14}^*S_{42}\right|^2}{\left[1 - \left(|S_{11}|^2 + |S_{21}|^2 + |S_{31}|^2 + |S_{41}|^2\right)\right]\left[1 - \left(|S_{12}|^2 + |S_{22}|^2 + |S_{32}|^2 + |S_{42}|^2\right)\right]}. \tag{6}$$

Using measured *S*-parameters, the calculated ECC values of the air-, gypsum-, and plywood-design arrays were shown in figures 18(a)–(c), respectively. For the operating band, all the ECC values were lower than 0.001, showing a low correlation between elements.

4.3.3. Diversity gain
DG is another significant metric of MIMO performance, which evaluates the received signal-to-noise-ratio improvement obtained from a multi-antenna system relative to a single antenna system in one diversity channel [42, 44]. The DG is mathematically relevant to the ECC [45], which can be approximated by

$$\mathrm{DG} = 10 \times \sqrt{1 - |0.99\rho_{\mathrm{e}}|}. \tag{7}$$

The calculated DG values of the air-, gypsum-, and plywood-design arrays are shown in figures 18(d)–(f), respectively. All the DG values were higher than 9.95 dB at the operating frequency, which ensured the diversity performance of the arrays.

4.3.4. Mean effective gain and power ratio factor
The MEG measures the ratio of the average power received at the port *i* of a *N*-element antenna array over the mean incident power of the array in the fading propagation environment [46]. Assuming that the propagation environment is uniform, Rayleigh, the MEG for antenna port *i*, can be calculated using *S*-parameters [47, 48]

$$\mathrm{MEG}_i = 0.5 \left(1 - \sum_{j=1}^{N} |S_{ij}|^2\right). \tag{8}$$

The magnitude difference of the MEG values for port *i* and *j* is expressed by the power ratio factor

$$k_{ij} = k_{ji} = \left|\mathrm{MEG}_i - \mathrm{MEG}_j\right|. \tag{9}$$

For reaching almost equal power ratios for all ports, *k* should be less than 3 dB [48]. Using the measured *S*-parameters, the calculated MEG and power ratio factors of the proposed three arrays are shown in figure 19. For the operating frequency, all the MEG values were lower than −3 dB, and the power ratio factors were lower than 0.5 dB.
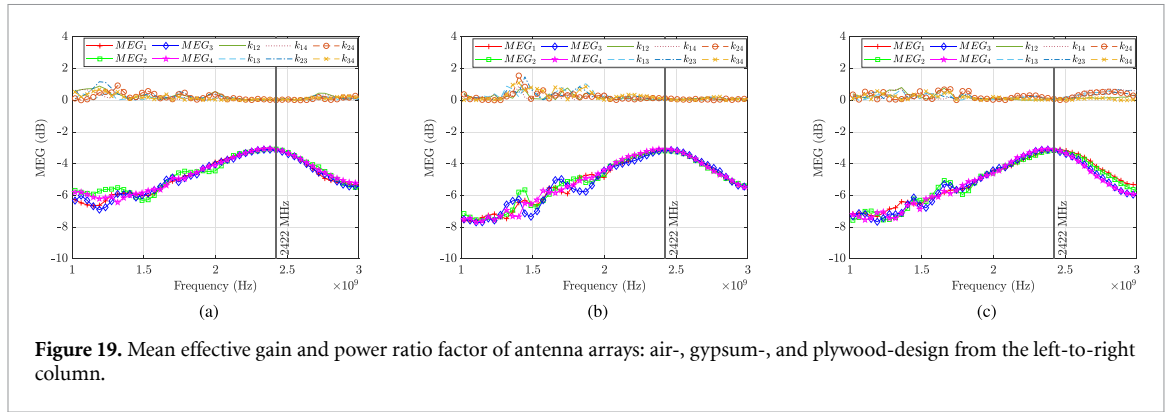
Figure 19. Mean effective gain and power ratio factor of antenna arrays: air-, gypsum-, and plywood-design from the left-to-right column.
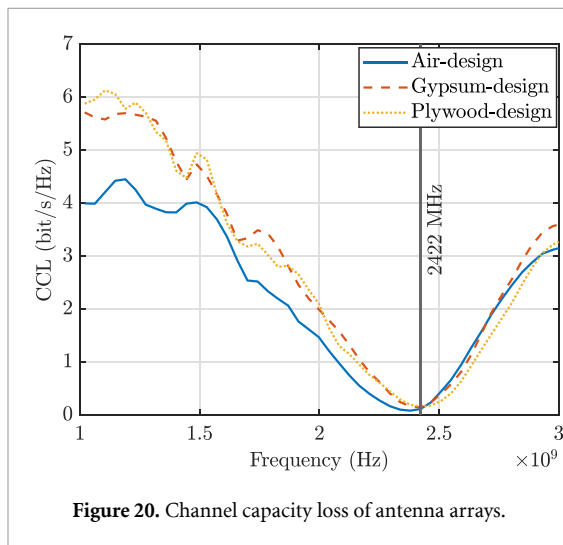

Figure 20. Channel capacity loss of antenna arrays.

4.3.5. Channel capacity loss

In MIMO antenna systems, the CCL evaluates the maximum rate of reliable information transmission over the communication channel [49, 50], expressed by

$$C = -\log_2 \det\left(\mathbf{\Psi}^R\right), \tag{10}$$

where $\mathbf{\Psi}^R$ is the correlation matrix of N-element receiving antenna array

$$\mathbf{\Psi}^R = \begin{bmatrix} \rho_{11} & \cdots & \rho_{1N} \\ \vdots & \ddots & \vdots \\ \rho_{N1} & \cdots & \rho_{NN} \end{bmatrix}, \tag{11}$$

where $\rho_{ii} = 1 - \sum_{n=1}^{N} |S_{in}|^2$ and $\rho_{ij} = -\left(S_{ii}^* S_{ij} + S_{ji}^* S_{ij}\right)$ for $i, j = 1, 2, \ldots, N$. For the proposed three arrays, the CCL values were calculated using measured S-parameters, providing losses less than 0.4 bits/s/Hz, shown in figure 20.

In this sub-section, the proposed three antenna arrays were evaluated in terms of several MIMO antenna diversity performance metrics using the measured S-parameters. The results indicate that the

diversity performance of our antenna arrays can be expected.

5. Conclusions

In this paper, CPW patch antennas and antenna arrays are designed and characterized with commonly used background wall materials, i.e., gypsum and plywood. For classification purposes, they were named as air, gypsum and plywood designs. The fabrication was thereafter realized with the inkjet printing technique, which resulted in flexible, lightweight, and low-cost specimens. For the air-design antenna, the measurement of the S_{11} parameter and the radiation pattern were deduced to be in agreement with the simulation results. The measured resonance frequency of this design was in the 2.4 GHz ISM band with a bandwidth of 340 MHz for a return loss level of 10 dB, demonstrating a peak gain of 0.93 dBi. Moreover, the gypsum- and plywood-design antennas also demonstrated resonance frequencies around 2.4 GHz with bandwidths beyond 340 MHz for a return loss level of 10 dB. With them being attached to their corresponding background materials, the peak gains of gypsum- and plywood-designs were 1.83 dBi and 1.00 dBi, respectively. The designed antennas demonstrated efficiency values that were above 50% around the operating frequency band.

Based on these three antenna designs, three 1×4 antenna arrays were fabricated and investigated. As a benchmark case, first, the air-design array was investigated. The measurement of the radiation pattern for the array design was in agreement with the simulation results, demonstrating a significantly higher peak gain of 6.54 dBi compared to the single antenna design. The gypsum- and plywood-designed arrays also provided similar radiation patterns with respective peak gains of 7.06 dBi and 6.13 dBi. By implementing the gypsum- and plywood-design arrays, it was possible to compensate for the radiation shift issue, which was observed during the single antenna measurements. The arrays provided efficiency values above

50% around the operating frequency band. Furthermore, the measured *S*-parameters indicate that the elements of each array have return losses beyond 15 dB and isolation more than 20 dB. By calculating the measured *S*-parameters, all three arrays provide a diversity performance in terms of ECC (ECC < 0.001), DG (DG > 9.95 dB), MEG (MEG < −3 dB), power ratio factor ($k < 0.5$ dB), and CCL (CCL < 0.4 bits/s/Hz) which ensure their MIMO performance for various wireless applications. Therefore, printed antennas and antenna arrays have been proven to be implemented in short-range radio transmission scenarios, such as IoT, backscatter communications, and wireless sensing applications for the indoor scenarios. In future work, these scenarios with the introduced designs will be investigated and further development and application possibilities will be sought after.

Data availability statement

All data that support the findings of this study are included within the article (and any supplementary files).

Acknowledgments

ORCID iDs

Juho Kerminen ⬤ https://orcid.org/0000-0003-0394-4704
Boxuan Xie ⬤ https://orcid.org/0000-0002-3175-3959
Lauri Mela ⬤ https://orcid.org/0000-0001-8669-6157
Alp Karakoç ⬤ https://orcid.org/0000-0002-2010-9607
Kalle Ruttik ⬤ https://orcid.org/0000-0002-7365-9194
Riku Jäntti ⬤ https://orcid.org/0000-0002-5398-2381

References

[1] Tobjörk D and Österbacka R 2011 Paper electronics *Adv. Mater.* **23** 1935–61
[2] Matyas J, Munster L, Olejnik R, Vlcek K, Slobodian P, Krcmar P, Urbanek P and Kuritka I 2016 Antenna of silver nanoparticles mounted on a flexible polymer substrate constructed using inkjet print technology *Jpn. J. Appl. Phys.* **55** 02BB13
[3] Jilani S F and Alomainy A 2016 Planar millimeter-wave antenna on low-cost flexible pet substrate for 5g applications *2016 10th European Conf. on Antennas and Propagation (EuCAP)* pp 1–3
[4] Shafique K, Khawaja B A, Khurram M D, Sibtain S M, Siddiqui Y, Mustaqim M, Chattha H T and Yang X 2018 Energy harvesting using a low-cost rectenna for internet of things (IoT) applications *IEEE Access* **6** 30932–41
[5] Shahidul Islam M, Islam M T, Ullah M A, Kok Beng G, Amin N and Misran N 2019 A modified meander line microstrip patch antenna with enhanced bandwidth for 2.4 GHz ism-band internet of things (IoT) applications *IEEE Access* **7** 127850–61
[6] Wiklund J, Karakoç A, Palko T, Yiğitler H, Ruttik K, Jäntti R and Paltakari J 2021 A review on printed electronics: fabrication methods, inks, substrates, applications and environmental impacts *J. Manuf. Mater. Process.* **5** 89
[7] Marasco I, Niro G, Mastronardi V, Rizzi F, D'Orazio A, De Vittorio M and Grande M 2022 A compact evolved antenna for 5g communications *Sci. Rep.* **12** 1–11
[8] Kerminen J, Wiklund J, Karakoç A, Ruttik K, Jäntti R and Yiğitler H 2021 Characterization of low-cost inkjet printed-photonic cured strain gauges for remote sensing and structural monitoring applications *Res. Eng. Struct. Mater.* **7** 14
[9] Khaleel H R, Al-Rizzo H M, Rucker D G and Mohan S 2012 A compact polyimide-based uwb antenna for flexible electronics *IEEE Antennas Wirel. Propag. Lett.* **11** 564–7
[10] Casula G A, Montisci G and Mazzarella G 2013 A wideband pet inkjet-printed antenna for uhf rfid *IEEE Antennas Wirel. Propag. Lett.* **12** 1400–3
[11] Kazani I, Declercq F, Scarpello M L, Hertleer C, Rogier H, Ginste D V, Mey G D, Guxho G and Langenhove L V 2014 Performance study of screen-printed textile antennas after repeated washing *Autex Res. J.* **14** 47–54
[12] Adami S-E, Zhu D, Li Y, Mellios E, Stark B H and Beeby S 2015 A 2.45 GHz rectenna screen-printed on polycotton for on-body rf power transfer and harvesting *2015 IEEE Wireless Power Transfer Conf. (WPTC)* pp 1–4
[13] Islam M T, Alam T, Yahya I and Cho M 2018 Flexible radio-frequency identification (rfid) tag antenna for sensor applications *Sensors* **18** 4212
[14] Li J, Jiang Y and Zhao X 2019 Circularly polarized wearable antenna based on ninjaflex-embedded conductive fabric *Int. J. Antennas Propag.* **2019** 1–8
[15] Yin X, Chen S J and Fumeaux C 2020 Wearable dual-band dual-polarization button antenna for wban applications *IEEE Antennas Wirel. Propag. Lett.* **19** 2240–4
[16] Zhang Y, Shen S, Chiu C-Y and Murch R 2020 A broadband transparent antenna integrated with an indoor solar cell for wlan applications *2020 IEEE Int. Symp. on Antennas and Propagation and North American Radio Science Meeting* pp 437–8
[17] Labiano I I and Alomainy A 2021 Flexible inkjet-printed graphene antenna on kapton *Flex. Print. Electron.* **6** 025010
[18] Shastri A, Sanz-Izquierdo B and Gao S 2022 Manufacturing considerations for the development of reconfigurable antennas using inexpensive inkjet printing *IEEE Trans. Compon. Packag. Manuf. Technol.* **12** 1021–8
[19] Sindhu B, Adepu V, Sahatiya P and Nandi S 2022 An mxene based flexible patch antenna for pressure and level sensing applications *FlatChem* **33** 100367
[20] Abutarboush H F 2022 Silver nanoparticle inkjet-printed multiband antenna on synthetic paper material for flexible devices *Alex. Eng. J.* **61** 6349–55
[21] Saha T K, Knaus T N, Khosla A and Sekhar P K 2022 A cpw-fed flexible uwb antenna for IoT applications *Microsyst. Technol.* **28** 5–11
[22] Biswas A K and Chakraborty U 2019 A compact wide band textile mimo antenna with very low mutual coupling for wearable applications *Int. J. RF Microw. Comput.-Aided Eng.* **29** e21769

[23] Monne M A, Grubb P M, Stern H, Subbaraman H, Chen R T and Chen M Y 2020 Inkjet-printed graphene-based 1 × 2 phased array antenna *Micromachines* **11** 863

[24] Khinda G S, Umar A, Cadwell R J, Alhendi M, Stoffel N C, Borgesen P and Poliks M D 2020 Flexible inkjet-printed patch antenna array on mesoporous pet substrate for 5g applications with stable rf performance after mechanical stress cycling *2020 IEEE 70th Electronic Components and Technology Conf. (ECTC)* pp 1824–31

[25] Lopez-Garde J-M, Del-Rio-Ruiz R, Legarda J and Rogier H 2021 2 × 2 textile rectenna array with electromagnetically coupled microstrip patch antennas in the 2.4 GHz wifi band *Electronics* **10** 1447

[26] Elmobarak H A, Himdi M, Castel X, Rahim S K A and Geok T K 2022 Flexible patch antenna array operating at microwaves based on thin composite material *IEEE Access* **10** 115663–72

[27] Dey A B, Pattanayak S S, Mitra D and Arif W 2021 Investigation and design of enhanced decoupled uwb mimo antenna for wearable applications *Microw. Opt. Technol. Lett.* **63** 845–61

[28] Jayant S, Srivastava G and Kumar S 2022 Quad-port uwb mimo footwear antenna for wearable applications *IEEE Trans. Antennas Propag.* **70** 7905–13

[29] Palazzi V, Su W, Bahr R, Bittolo-Bon S, Alimenti F, Mezzanotte P, Valentini L, Tentzeris M M and Roselli L 2019 3-d-printing-based selective-ink-deposition technique enabling complex antenna and rf structures for 5g applications up to 6 GHz *IEEE Trans. Compon. Packag. Manuf. Technol.* **9** 1434–47

[30] Rosker E S, Sandhu R, Hester J, Goorsky M S and Tice J 2018 Printable materials for the realization of high performance rf components: challenges and opportunities *Int. J. Antennas Propag.* **2018** 9359528

[31] Loss C, Gonçalves R, Lopes C, Pinho P and Salvado R 2016 Smart coat with a fully-embedded textile antenna for IoT applications *Sensors* **16** 938

[32] Ahmed S, Tahir F A, Shamim A and Cheema H M 2015 A compact kapton-based inkjet-printed multiband antenna for flexible wireless devices *IEEE Antennas Wirel. Propag. Lett.* **14** 1802–5

[33] Mohamadzade B, Hashmi R M, Simorangkir R B V B, Gharaei R, Ur Rehman S and Abbasi Q H 2019 Recent advances in fabrication methods for flexible antennas in wearable devices: state of the art *Sensors* **19** 2312

[34] Beisteiner C and Zagar B G 2016 Dielectric permittivity measurement of paper substrates using commercial inkjet printers *Proc. Eng.* **168** 995–8

[35] Brinker K R 2019 Passively-coded embedded microwave sensors for materials characterization and structural health monitoring (SHM) *Master Thesis* Missouri University of Science and Technology

[36] Das N K, Voda S M and Pozar D M 1987 Two methods for the measurement of substrate dielectric constant *IEEE Trans. Microw. Theory Tech.* **35** 636–42

[37] Balanis C A 2015 *Antenna Theory: Analysis and Design* (New York: Wiley)

[38] Khatun M H, Inum R and Tasnim N 2017 Design of rectangular patch antenna array using different feeding technique *2017 2nd Int. Conf. on Electrical & Electronic Engineering (ICEEE)* pp 1–4

[39] Schroder K, Rawson I M, Pope D S and Farnsworth S 2011 Photonic curing explanation and application to printing copper traces on low temperature substrates *Int. Symp. on Microelectronics* vol 2011 (International Microelectronics Assembly and Packaging Society) pp 001040–6

[40] Keysight Technologies *Advanced Design System Documentation* (available at: https://edadocs.software. keysight.com/display/ads201101/PDF+Files+for+ ADS+Documentation)

[41] Papamichael V, Karaboikis M, Soras C and Makios V 2007 Diversity and mimo performance evaluation of compact multi element antennas with common phase center *2007 19th Int. Conf. on Applied Electromagnetics and Communications* pp 1–4

[42] Vaughan R and Andersen J 1987 Antenna diversity in mobile communications *IEEE Trans. Veh. Technol.* **36** 149–72

[43] Blanch S, Romeu J and Corbella I 2003 Exact representation of antenna system diversity performance from input parameter description *Electron. Lett.* **39** 705–7

[44] Sharawi M S 2013 Printed multi-band mimo antenna systems and their performance metrics [wireless corner] *IEEE Antennas Propag. Mag.* **55** 218–32

[45] Rosengren K and Kildal P-S 2005 Radiation efficiency, correlation, diversity gain and capacity of a six-monopole antenna array for a mimo system: theory, simulation and measurement in reverberation chamber *IEE Proc.* **152** 7–16

[46] Ko S and Murch R 2001 Compact integrated diversity antenna for wireless communications *IEEE Trans. Antennas Propag.* **49** 954–60

[47] Kalliola K, Sulonen K, Laitinen H, Kivekas O, Krogerus J and Vainikainen P 2002 Angular power distribution and mean effective gain of mobile antenna in different propagation environments *IEEE Trans. Veh. Technol.* **51** 823–38

[48] Nasir J, Jamaluddin M H, Khalily M, Kamarudin M R, Ullah I and Selvaraju R 2015 A reduced size dual port mimo dra with high isolation for 4g applications *Int. J. RF and Microw. Comput.-Aided Eng.* **25** 495–501

[49] Chae S H, Oh S-k and Park S-O 2007 Analysis of mutual coupling, correlations and tarc in wibro mimo array antenna *IEEE Antennas Wirel. Propag. Lett.* **6** 122–5

[50] See C H, Abd-Alhameed R A, Abidin Z Z, McEwan N J and Excell P S 2012 Wideband printed mimo/diversity monopole antenna for wifi/wimax applications *IEEE Trans. Antennas Propag.* **60** 2028–35